



Multiple hypothesis template tracking of small 3D vessel structures

Ola Friman *, Milo Hindennach, Caroline Kühnel, Heinz-Otto Peitgen

Fraunhofer MEVIS, Universitätsallee 29, 28359 Bremen, Germany

ARTICLE INFO

Article history:

Received 1 November 2008
Received in revised form 7 October 2009
Accepted 8 December 2009
Available online 16 December 2009

Keywords:

Segmentation
Vessels
Tracking
Multiple hypothesis
Template model
Liver arteries
Coronary arteries

ABSTRACT

A multiple hypothesis tracking approach to the segmentation of small 3D vessel structures is presented. By simultaneously tracking multiple hypothetical vessel trajectories, low contrast passages can be traversed, leading to an improved tracking performance in areas of low contrast. This work also contributes a novel mathematical vessel template model, with which an accurate vessel centerline extraction is obtained. The tracking is fast enough for interactive segmentation and can be combined with other segmentation techniques to form robust hybrid methods. This is demonstrated by segmenting both the liver arteries in CT angiography data, which is known to pose great challenges, and the coronary arteries in 32 CT cardiac angiography data sets in the Rotterdam Coronary Artery Algorithm Evaluation Framework, for which ground-truth centerlines are available.

© 2009 Elsevier B.V. All rights reserved.

1. Introduction

Non-invasive Computed Tomography (CT) and Magnetic Resonance Imaging (MRI) angiography are increasingly replacing invasive angiography procedures for examining and visualizing vessels. A common objective is to detect vessel anomalies and pathologies such as aneurysms, stenoses, and plaques. CT and MRI angiography may also provide useful surgical planning information such as blood supply architecture and intra-operative navigation landmarks. To obtain an adequate vessel visualization, segmentation is often necessary. Extensive overviews of vessel segmentation procedures are given in Suri et al. (2002), Bühler et al. (2003), Kirbas and Quek (2004), Lesage et al. (2009). Practically all currently used vessel segmentation methods are based on a growth process emanating from an automatically- or user-defined starting point; the differences between methods lie in the constraints imposed on the growth process. A schematic overview of different vessel segmentation approaches are depicted in Fig. 1. In this figure, proposed segmentation methods are classified according to the model assumptions employed, which determine the vessel sizes and image contrasts to which they are best applied.

The simplest algorithm is a region growing (Adams and Bischof, 1994; O'Brien and Ezquerro, 1994; Wan and Higgins, 2003), which works well for highly contrasted vessels, but leaks into neighboring

non-vessel tissue where the contrast is low. To combat leakage, shape constraints and stronger vessel modeling must be applied. One approach is to enhance vessel-like structures in a pre-processing step (Sato et al., 1997; Frangi et al., 1998; Krissian, 2002; Cenero and Radeva, 2003; Manniesing et al., 2006). Another popular way is to introduce shape constraints via front propagation, curve evolution, and level-set techniques (Lorigo et al., 2001; Vasilevskiy and Siddiqi, 2002; Deschamps and Cohen, 2002; Nain et al., 2004; Manniesing and Niessen, 2004; Chen and Amini, 2004; Manniesing et al., 2006; Yan and Kassim, 2006; Yang et al., 2007; Gooya et al., 2007). The growth process in these methods is governed by a shape factor, e.g., the curvature of the growing front. The front propagation methods may encounter difficulties segmenting small vessel systems, as these exhibit high curvatures and irregularities that do not conform to the shape constraints. To push the detectable vessel size and contrast limit further, explicit vessel models may be employed within a tracking framework. Vessel tracking approaches assume the existence of a well-defined center line and identify vessels iteratively by estimating vessel parameters such as center line points and radius.

In Fig. 1, the tracking methods have been subdivided into ridge tracking, cross-section tracking, and tubular tracking. In a ridge tracking approach, vessels are modeled as intensity ridges that are tracked using either gradient information (Wink et al., 2000) or second-order information in the Hessian matrix (Aylward and Bullitt, 2002; McIntosh and Hamarneh, 2006). Minimal path approaches find a minimum cost path between two points (Deschamps and Cohen, 2001; Olabarriaga et al., 2003), where the cost can be defined by a vesselness measure based on the Hessian

* Corresponding author.

E-mail addresses: ola.friman@mevis.fraunhofer.de (O. Friman), milo.hindennach@mevis.fraunhofer.de (M. Hindennach), caroline.kuehnel@mevis.fraunhofer.de (C. Kühnel), peitgen@mevis.fraunhofer.de (H.-O. Peitgen).

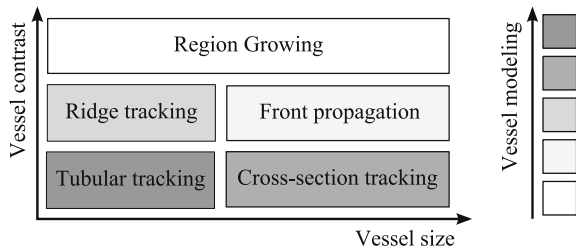


Fig. 1. Classification of vessel segmentation methods based on the degree of vessel modeling utilized. The strength and type of the vessel model determine the vessel size and contrast for which the method is best suited.

matrix (Sato et al., 1997; Frangi et al., 1998), a Gaussian model (Bhalerao et al., 2001), or non-parametric measures (Zambal et al., 2008). Differentiation is a noise-sensitive operation that may require more smoothing than is optimal for detecting small vessels. Explicit modeling of the vessel shape is required for segmenting very low contrast vessels. For example, modeling the vessel cross-section as an ellipse is commonplace (Noordmans and Smeulders, 1998; Behrens et al., 2003; Florin et al., 2005; Shim et al., 2006; Krissian et al., 2006), leading to the cross-section tracking in Fig. 1. For smaller vessels (<3 voxels in diameter), there may not be enough data to fit a 2D cross-section model, and edge information may not be reliable. The strongest form of modeling assumes that the vessel can locally be described as a linear tube segment, whereby a full 3D fitting becomes justified. Variations of this tubular tracking approach have recently been proposed (La Cruz et al., 2004; Tyrrell et al., 2007; Schaap et al., 2007; Lee et al., 2007; Rossignac et al., 2007; Wörz and Rohr, 2007; Wong and Chung, 2007). Hybrid approaches are also conceivable. For example, a level-set approach combined with a vessel topology model was recently proposed by Manniesing et al. (2007).

In this work, a tubular tracking algorithm based on 3D template matching is presented. Template matching is a classic and well-evaluated image processing concept that rests on the Matched Filter Theorem. For vessel tracking, the template is an image patch containing an idealized vessel segment parameterized by a radius, a center location, and a direction (Chaudhuri et al., 1989; Noordmans and Smeulders, 1998; La Cruz et al., 2004; Wörz and Rohr, 2007). In this work, a novel modular vessel template model is introduced along with a dedicated fitting procedure. In addition, a Multiple Hypothesis Tracking (MHT) procedure for vessels is presented. MHT is a concept from the signal processing and control theory communities which means that the tracking algorithm considers several possible trajectories or hypotheses simultaneously (Reid, 1979; Blackman, 2004). Originally, MHT was designed to relax the unimodal distribution restriction in the Kalman filter and to postpone difficult decisions until more data has been observed. In the proposed vessel tracking algorithm, the MHT concept is used to traverse difficult vessel passages such as pathologies and areas of low contrast. A preliminary presentation of the vessel tracking method has previously been published in (Friman et al., 2008). The presented methodology is demonstrated and evaluated using both synthetic data and real CT angiography data of the liver arteries and the coronary arteries.

2. Vessel template model

A vessel model is required to implement a vessel tracking algorithm. In the literature, a number of different models have been suggested, e.g., ridge models based on second-order derivatives (Aylward and Bullitt, 2002), elliptical cross-sections (Behrens et al., 2003; Florin et al., 2005; Shim et al., 2006; Krissian et al.,

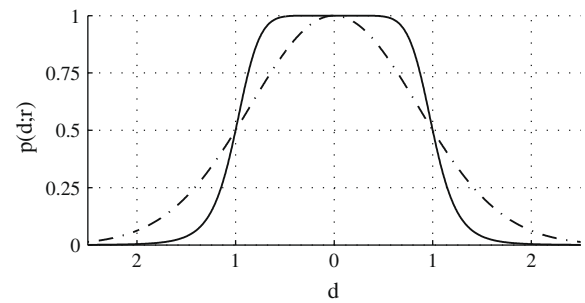


Fig. 2. The proposed vessel profile $p(d^2; r)$ with $r = 1$ is shown as a solid line. The dash-dotted line shows an equivalent Gaussian profile, which is more suitable for smoothed data. Note that both profiles attain the value 0.5 for $d = r$.

2006), spheres (Rossignac et al., 2007), superellipsoids (Tyrrell et al., 2007), and template models (Chaudhuri et al., 1989; Noordmans and Smeulders, 1998; La Cruz et al., 2004; Wörz and Rohr, 2007). In this work, a new tubular template model suitable for the segmentation of small vessel is introduced. The model is a template function $T(\mathbf{x}; r, \mathbf{x}_0, \hat{\mathbf{v}}) : \mathbb{R}^n \rightarrow [0, 1]$, which maps a spatial coordinate \mathbf{x} in \mathbb{R}^n to the interval $[0, 1]$. The template function is an idealized model of a local image neighborhood centered around the spatial center point \mathbf{x}_0 through which a vessel with radius r runs in the direction of the unit vector $\hat{\mathbf{v}}$. To cope with anisotropic voxels, we express the template in a world coordinate system, i.e., the unit of the parameters is millimeters. Moreover, the template has a circular cross-section. This choice is motivated by the fact that small vessels generally are round, and that at small scales, the difference between a circular and an elliptic cross-section is negligible. Related models in the literature include the oriented Gaussian ellipsoid model proposed by Noordmans and Smeulders (1998). Wörz and Rohr (2007) note that a Gaussian vessel profile generally does not describe vessels well and instead introduce a cylinder model smoothed with a Gaussian function as template model. A drawback of this model, however, is that it is mathematically intractable and approximations must be employed. Nevertheless, in Wörz and Rohr (2007), it is shown that the model yields more accurate results than a template with a Gaussian profile function. La Cruz et al. (2004) have introduced a similar cylinder model described by an implicit function and a step function convolved with a Gaussian function as radial vessel profile. Although mathematically tractable, a drawback of this model is that the distance to the cylinder surface is only estimated and not exactly calculated, which may affect accuracy. In the model described below, the template model is instead based on the exact Euclidian distance from a line in n D-space and the vessel radius enters as a parameter in a 1D vessel profile function.

2.1. Vessel profile

A 1D vessel profile function $p(d^2) : \mathbb{R} \rightarrow [0, 1]$, where d^2 is the squared distance to the vessel center, models the image intensity variation across the vessel. A Gaussian vessel profile has been used previously in Noordmans and Smeulders (1998) and Krissian et al. (2000). The Gaussian profile fits well when the image have been smoothed, but for small vessels, smoothing should be limited to preserve the high-frequency vessel structures, in which case a steeper vessel profile is required (see Fig. 1 in Wörz and Rohr (2007), for an example).

In this work, we propose the following vessel profile function:

$$p(d^2; r) = \frac{r^\gamma}{(d^2)^{\gamma/2} + r^\gamma} \quad \text{with } \gamma = 8 \quad (1)$$

which is depicted in Fig. 2. The γ parameter controls the steepness of the profile and its value is fixed in this work.

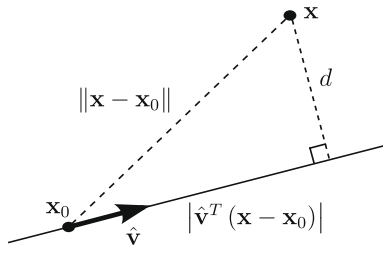


Fig. 3. The distance d from a point \mathbf{x} to a straight line parameterized by the center point \mathbf{x}_0 and direction $\hat{\mathbf{v}}$ is found via the Pythagorean theorem.

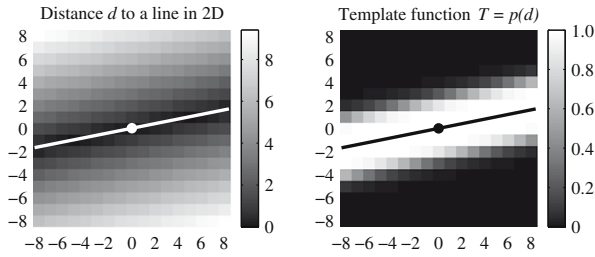


Fig. 4. Example of a vessel template in 2D. Left: Distance to a straight line parameterized by the center point \mathbf{x}_0 and direction $\hat{\mathbf{v}}$. Right: The template is obtained by applying the vessel profile function parameterized by the radius r to the distance function, cf. Eq. (4).

2.2. Distance to a line in \mathbb{R}^n

The second part of the template function is the minimum distance d from a point \mathbf{x} in \mathbb{R}^n to a line running in the direction $\hat{\mathbf{v}}$ through the point \mathbf{x}_0 , see Fig. 3. This distance is straightforwardly found via the Pythagorean theorem

$$\|\mathbf{x} - \mathbf{x}_0\|^2 = d^2 + [\hat{\mathbf{v}}^T(\mathbf{x} - \mathbf{x}_0)]^2 \quad (2)$$

where $\|\mathbf{x} - \mathbf{x}_0\|$ is the distance between \mathbf{x} and \mathbf{x}_0 , and $\hat{\mathbf{v}}^T(\mathbf{x} - \mathbf{x}_0)$ is the projection of the vector $(\mathbf{x} - \mathbf{x}_0)$ onto the unit vector $\hat{\mathbf{v}}$. We now make the squared distance d^2 a function

$$d^2(\mathbf{x}; \mathbf{x}_0, \hat{\mathbf{v}}) = \|\mathbf{x} - \mathbf{x}_0\|^2 - [\hat{\mathbf{v}}^T(\mathbf{x} - \mathbf{x}_0)]^2 \quad (3)$$

parameterized by the center point \mathbf{x}_0 and the direction $\hat{\mathbf{v}}$. This explains why the vessel profile function in Eq. (1) is a function of the squared distance; such a function avoids a square-root operation and gains some computational performance. Note that Eq. (3) is valid for any dimension, i.e., 2D, 3D, 4D, etc.

2.3. The vessel template

The vessel template function is defined as the composite of the functions $p(d^2; r)$ and $d^2(\mathbf{x}; \mathbf{x}_0, \hat{\mathbf{v}})$ defined in the previous sections:

$$T(\mathbf{x}; r, \mathbf{x}_0, \hat{\mathbf{v}}) = p \circ d^2(\mathbf{x}) = p(d^2(\mathbf{x}; \mathbf{x}_0, \hat{\mathbf{v}}); r). \quad (4)$$

An example of a 2D vessel template generation is shown in Fig. 4. Again, note that the vessel template function is general in that it can produce templates of arbitrary dimension and with any vessel profile function.

3. Image model and vessel template fitting

In this section, we describe how the template function $T(\mathbf{x}; r, \mathbf{x}_0, \hat{\mathbf{v}})$, presented above, is fitted to observed image data. Be-

fore presenting the fitting procedure, an image model and a weight function that spatially localizes the fit are introduced.

3.1. Image model

A local image neighborhood $I(\mathbf{x})$, where $\mathbf{x} \in \mathbb{R}^n$ is a spatial coordinate, is modeled as

$$I(\mathbf{x}) = kT(\mathbf{x}; r, \mathbf{x}_0, \hat{\mathbf{v}}) + m + \epsilon(\mathbf{x}) \quad (5)$$

where k is the vessel contrast and m is the image background intensity. The remaining term $\epsilon(\mathbf{x})$ represents noise and interfering surrounding structures. In the following sections, we refer to k and m as *image parameters* and to the template parameters r, \mathbf{x}_0 , and $\hat{\mathbf{v}}$ as *vessel parameters*.

3.2. Weight function

To localize the fit of the vessel template to a certain area of the image, the following Gaussian weight function is used:

$$w(\mathbf{x}; r, \mathbf{x}_0, \hat{\mathbf{v}}) = e^{-\frac{(\hat{\mathbf{v}}^T(\mathbf{x} - \mathbf{x}_0))^2}{(2r)^2} - \frac{(\hat{\mathbf{u}}_1^T(\mathbf{x} - \mathbf{x}_0))^2 + (\hat{\mathbf{u}}_2^T(\mathbf{x} - \mathbf{x}_0))^2}{(4r)^2}} \quad (6)$$

where $\hat{\mathbf{u}}_1$ and $\hat{\mathbf{u}}_2$ are unit vectors that are orthogonal to both $\hat{\mathbf{v}}$ and to each other, i.e., $\hat{\mathbf{v}} \perp \hat{\mathbf{u}}_1 \perp \hat{\mathbf{u}}_2$, viz. $\hat{\mathbf{u}}_1$ and $\hat{\mathbf{u}}_2$ span the plane to which $\hat{\mathbf{v}}$ is the normal vector. The choice of $\hat{\mathbf{u}}_1$ and $\hat{\mathbf{u}}_2$ is not unique; any pair perpendicular to both each other and $\hat{\mathbf{v}}$ will suffice. The weight function is centered on the vessel template center \mathbf{x}_0 and its width is determined by the vessel radius r . Moreover, the weight function is anisotropic and broader across the vessel (along the directions $\hat{\mathbf{u}}_1$ and $\hat{\mathbf{u}}_2$) than along the vessel direction $\hat{\mathbf{v}}$ so as to better conform to the locally linear vessel segment assumption. We denote by $\mathbf{x}_i, i = 1, \dots, n$ all voxel locations for which $w(\mathbf{x}_i; r, \mathbf{x}_0, \hat{\mathbf{v}}) > 0.05$ and only these voxels are considered when fitting the vessel template. Similar weight functions have previously been used in Noordmans and Smeulders (1998) and Wörz and Rohr (2007).

3.3. Vessel template fitting

To fit the image and vessel parameters to the image data, the following weighted least-squares problem is solved:

$$\min_{r, \mathbf{x}_0, \hat{\mathbf{v}}, k, m} \|\mathbf{W}(r, \mathbf{x}_0, \hat{\mathbf{v}})[k\mathbf{T}(r, \mathbf{x}_0, \hat{\mathbf{v}}) + m\mathbf{1}_n - \mathbf{I}]\|^2 \quad (7)$$

where \mathbf{I} and $\mathbf{T}(r, \mathbf{x}_0, \hat{\mathbf{v}})$ are $(n \times 1)$ vectors containing the image data and template values for the spatial locations $\mathbf{x}_i, i = 1 \dots n$, i.e., the voxels under the weight function. $\mathbf{W}(r, \mathbf{x}_0, \hat{\mathbf{v}})$ is a diagonal matrix with the corresponding weights, and $\mathbf{1}_n$ is a constant $(n \times 1)$ vector. Note that the least-squares problem is linear in the image parameters k and m but nonlinear in the vessel parameters. This is known as a separable nonlinear least-squares problem, and a solution can be found by an iteration in which the linear parameters are solved while keeping the nonlinear parameters constant and vice versa (Björck, 1996). Details are given below.

3.3.1. Fitting the image parameters k and m

To find the vessel contrast k and mean image intensity m , the following $(n \times 2)$ -matrix is introduced:

$$\mathbf{X} = \begin{bmatrix} T(\mathbf{x}_1; r, \mathbf{x}_0, \hat{\mathbf{v}}) & 1 \\ \vdots & \vdots \\ T(\mathbf{x}_n; r, \mathbf{x}_0, \hat{\mathbf{v}}) & 1 \end{bmatrix} \quad (8)$$

i.e., a column with the template values calculated with the current values of the vessel parameters and a column of ones. The optimal image parameter values are then found via the normal equations

$$\begin{bmatrix} k \\ m \end{bmatrix} = (\mathbf{X}^T \mathbf{W}^2 \mathbf{X})^{-1} \mathbf{X}^T \mathbf{W}^2 \mathbf{I} \quad (9)$$

3.3.2. Fitting the vessel parameters r , \mathbf{x}_0 and $\hat{\mathbf{v}}$

The Levenberg–Marquardt algorithm is a popular method for solving nonlinear least-squares problems (Gill and Murray, 1978), which has also previously been used for fitting vessel models (La Cruz et al., 2004; Wörz and Rohr, 2007). Only a brief outline of the Levenberg–Marquardt method is given here and the reader is referred to the extensive literature on the topic for further details. The first necessary component is the $(n \times 1)$ residual vector from Eq. (7):

$$\mathbf{r} = k\mathbf{T}(r, \mathbf{x}_0, \hat{\mathbf{v}}) + m\mathbf{1}_n - \mathbf{I} \quad (10)$$

which indicates the mismatch between the image and the vessel template with the current parameter values. To improve the template fit, we try to find small corrections of the vessel radius, rotation, and translation. To this end, it is convenient to use a spherical representation of the vessel direction

$$\hat{\mathbf{v}}(\theta, \phi) = \begin{bmatrix} \sin(\phi) \cos(\theta) \\ \sin(\phi) \sin(\theta) \\ \cos(\phi) \end{bmatrix} \quad (11)$$

where θ is the azimuth angle in the xy -plane from the x -axis ($0 \leq \theta < 2\pi$) and ϕ is the polar angle from the z -axis ($0 \leq \phi \leq \pi$). A rotation is now simply a change in θ and ϕ . Furthermore, we note that a translation of the vessel template along the direction $\hat{\mathbf{v}}$ will not change the template appearance. Hence, a change in \mathbf{x}_0 will only have an effect if it is orthogonal to $\hat{\mathbf{v}}$, i.e., along the unit vectors $\hat{\mathbf{u}}_1$ and $\hat{\mathbf{u}}_2$ introduced above in Section 3.2. To summarize, in 3D space, the vessel template can be changed along 5 degrees of freedom: the radius, 2 angles and 2 translation directions. For 2D tracking, there are 3 degrees of freedom: the radius, 1 angle and 1 translation direction. The $(n \times 5)$ Jacobian matrix containing the derivatives is

$$\mathbf{J} = k \left[\frac{\partial \mathbf{T}}{\partial r}, \frac{\partial \mathbf{T}}{\partial \theta}, \frac{\partial \mathbf{T}}{\partial \phi}, \hat{\mathbf{u}}_1^T \left(\frac{\partial \mathbf{T}}{\partial \mathbf{x}_0} \right), \hat{\mathbf{u}}_2^T \left(\frac{\partial \mathbf{T}}{\partial \mathbf{x}_0} \right) \right] \quad (12)$$

where $\hat{\mathbf{u}}_1^T \left(\frac{\partial \mathbf{T}}{\partial \mathbf{x}_0} \right)$ and $\hat{\mathbf{u}}_2^T \left(\frac{\partial \mathbf{T}}{\partial \mathbf{x}_0} \right)$ are the projections of a translation of \mathbf{x}_0 onto the orthogonal directions $\hat{\mathbf{u}}_1$ and $\hat{\mathbf{u}}_2$. Analytical expressions of the derivatives in Eq. (12) can be found in the appendix.

Trial increments of the radius (Δr), rotation angles ($\Delta \theta$ and $\Delta \phi$), and translations ($\Delta t_{\hat{\mathbf{u}}_1}$ and $\Delta t_{\hat{\mathbf{u}}_2}$) orthogonal to the vessel direction are found by solving a linear least-squares problem. Again, the solution is given by the normal equations:

$$[\Delta r, \Delta \theta, \Delta \phi, \Delta t_{\hat{\mathbf{u}}_1}, \Delta t_{\hat{\mathbf{u}}_2}]^T = (\mathbf{J}^T \mathbf{W}^2 \mathbf{J} + \tau \mathbf{I}_5) \mathbf{J}^T \mathbf{W}^2 \mathbf{r} \quad (13)$$

Particular to the Levenberg–Marquardt algorithm is the regularization factor $\tau \geq 0$ which is added to the diagonal via the (5×5) unit matrix \mathbf{I}_5 . For a large enough τ , there is always a parameter update $r \leftarrow r + \Delta r$, $\theta \leftarrow \theta + \Delta \theta$, $\phi \leftarrow \phi + \Delta \phi$ and $\mathbf{x}_0 \leftarrow \mathbf{x}_0 + \Delta t_{\hat{\mathbf{u}}_1} \hat{\mathbf{u}}_1 + \Delta t_{\hat{\mathbf{u}}_2} \hat{\mathbf{u}}_2$ that improves the fit. To find such an update, one starts with a small τ and gradually increases it until Eq. (13) delivers an updated vessel template that decreases the squared sum of the residuals in Eq. (10). If the norm of the solution vector in Eq. (13) is smaller than a pre-defined constant, the optimization has converged.

3.4. Vessel template significance

For tracking purposes, e.g., to determine when to terminate the tracking, we need to evaluate how well a template fits the image data. That is, we ask how well the image data support the hypothesis of the existence of a vessel with radius r at spatial location \mathbf{x}_0 running in direction $\hat{\mathbf{v}}$. To test this hypothesis, we investigate if the

estimated vessel contrast k is significantly different from zero. A classical way of doing this is to calculate a Student's t -statistic $t(k)$

$$t(k) \triangleq \frac{k - 0}{\text{std}(k)} = \frac{k}{\text{std}(k)} \quad (14)$$

where $\text{std}(k)$ is the standard error, i.e., the square-root of the variance, of the estimator of k . Essentially, Eq. (14) is a contrast-to-noise ratio for the vessel template. The vessel contrast is estimated in Eq. (9), in which we introduce the vector $\mathbf{c} = [1, 0]^T$, indicating that k is the first component. It can be shown that the standard error is obtained as (Draper and Smith, 1998)

$$\text{std}(k) = \sqrt{\sigma^2 \mathbf{c}^T (\mathbf{X}^T \mathbf{W}^2 \mathbf{X})^{-1} \mathbf{X}^T \mathbf{W}^4 \mathbf{X} (\mathbf{X}^T \mathbf{W}^2 \mathbf{X})^{-1} \mathbf{c}} \quad (15)$$

where \mathbf{W} is the weight matrix and \mathbf{X} is defined in Eq. (8). Assuming that the image noise is Gaussian and spatially independent, a Student's t -statistic with value $t(k) > 3$ can be considered significant. In general, however, noise in medical images is not spatially independent, but rather has a correlation that is described by the point-spread-function. This decreases the estimated variance of k in Eq. (15), which in turn inflates the t -score in Eq. (14). Therefore, as a rule of thumb, a suitable tracking termination threshold for $t(k)$ lies in the range 3–8 depending on the application.

4. Vessel tracking

The goal of a vessel tracking algorithm is to generate a chain of segments $\beta_0 \rightarrow \beta_1 \rightarrow \beta_2 \rightarrow \dots$ that describes the vessel, where β_t denotes a set of model parameters. For the vessel template model described in the previous section we have $\beta = \{r, \mathbf{x}_0, \hat{\mathbf{v}}, k, m\}$. The process of going from β_t to β_{t+1} involves a prediction step and a fitting step. Several tracking algorithms for 3D vessels have been proposed (Noordmans and Smeulders, 1998; Wink et al., 2000; Aylward and Bullitt, 2002; Behrens et al., 2003; La Cruz et al., 2004; Florin et al., 2005; McIntosh and Hamarneh, 2006; Shim et al., 2006; Krissian et al., 2006; Tyrrell et al., 2007; Schaap et al., 2007; Lee et al., 2007; Rossignac et al., 2007; Wörz and Rohr, 2007). These algorithms differ with regard to the vessel model and how prediction and update steps are done. Commonly, a prediction is placed along the tangential line (Noordmans and Smeulders, 1998; Wink et al., 2000; Aylward and Bullitt, 2002; La Cruz et al., 2004; Tyrrell et al., 2007; Lee et al., 2007; Rossignac et al., 2007; Wörz and Rohr, 2007). Aylward and Bullitt (2002) and Lee et al. (2007) then corrects the prediction by searching for the point of maximum vesselness in an orthogonal plane. Noordmans and Smeulders (1998), La Cruz et al. (2004), Tyrrell et al. (2007), Rossignac et al. (2007), and Wörz and Rohr (2007) instead fit parametric vessel segment models at the new position to improve the prediction. The Kalman filter, which has been employed for vessel tracking by Behrens et al. (2003) and Wörz and Rohr (2007), offers a similar but more principled tracking framework. However, the linear Kalman filter uses unimodal probability distributions and linear observation models, and is therefore not able to test alternative paths in difficult situations, such as in an area of low contrast or at the branching point of a vessel. To overcome these limitations, nonlinear Kalman filtering, so-called particle filtering, has recently been suggested for the vessel segmentation problem by Florin et al. (2005), Shim et al. (2006), and Schaap et al. (2007). The advantage of this approach is that multiple possible paths are simultaneously updated using nonlinear observation models, yielding improved robustness and accuracy. Although particle filtering is a competent tracking approach, it relies on a computationally intensive modeling of probability distributions in the form of a large number of particles. Dynamic programming approaches, such as the one introduced by Miles and Nuttall (1993) for the segmentation of 2D vessels, effectively also consider multi-

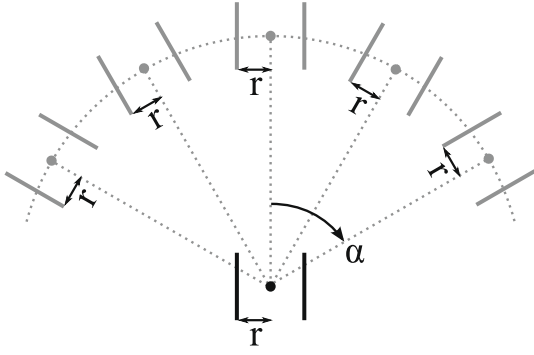


Fig. 5. Predictions of the next step are generated by keeping the radius r fixed and systematically sampling the area in front of the current position in $\pm\alpha$ degrees relative to the current vessel direction $\hat{\mathbf{v}}$. In 3D, a sphere segment is sampled.

ple paths. However, in a dynamic programming approach, the user is required to supply both a start point and an end point, and bifurcations will not be detected. The Multiple Hypothesis Tracking (MHT) concept (Reid, 1979), proposed in this work for the vessel tracking, also tracks multiple paths, but utilizes a more efficient non-stochastic sampling approach compared to a particle filter.

4.1. Step prediction

To capture potential branching and to test alternative paths in low contrast areas, a range of systematically placed predictions is evaluated in this work as illustrated in Fig. 5. Formally, a collection of possible vessel continuations $\beta_{t+1}^{(i)}$, $i = 1, 2, \dots$ is generated based on the current vessel segment β_t . These predictions are evenly placed on the circle segment or sphere segment defined by a $\pm\alpha^\circ$ angle from the current vessel direction $\hat{\mathbf{v}}$. All other vessel parameters, such as the radius, are kept constant in the prediction step. The step is set to 1.5 times the current radius. Each prediction has an associated score $s(\beta_{t+1}^{(i)})$, which serves as a basis for the further selection and processing. For the vessel template model used in this work, the score function presented in Section 3.4 is used.

4.2. Evaluating multiple hypotheses

In a single-hypothesis mode, a greedy strategy is employed, meaning that the prediction with the highest score is selected as the best path to pursue. However, the best local selection is not guaranteed to follow the correct global path. To optimize the trajectory over several steps, multiple predictions or hypotheses are tracked simultaneously in the MHT method. To select which predictions to pursue from the current point β_t , the pattern of prediction scores is investigated, see Fig. 6. The score pattern will normally contain one maximum that lies close to the true vessel trajectory, but multiple local maxima may occur in problematic regions in which the exact vessel path is unclear. In the MHT method, all predictions that exhibit a local maximum in the score pattern are taken as hypotheses of the vessel path. Possible paths are then recursively investigated as illustrated in Fig. 7. Assume that the current vessel segment is parameterized by β_t . The predictions for the next step exhibit two local score maxima, $\beta_{t+1}^{(1)}$ and $\beta_{t+1}^{(2)}$. Instead of immediately choosing one prediction to pursue, we continue to track from both predictions. By iterating the procedure, a tree each built in which the leaves $\beta_{t+3}^{(j)}$, $j = 1 \dots 6$ represent possible vessel trajectories. The depth of the tracking tree is denoted the *search depth*. When a pre-determined search depth has been reached, we decide where to go from β_t by calculating the average scores along the paths leading to each leaf $\beta_{t+3}^{(j)}$, $j = 1 \dots 6$ and taking a step towards the leaf with the highest score.

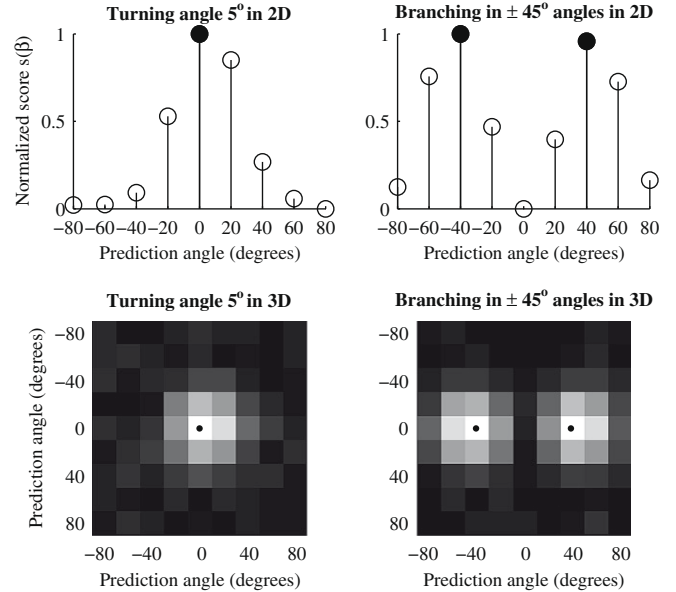


Fig. 6. The prediction scores $s(\beta_{t+1}^{(i)})$, $i = 1, 2, \dots$ as 1D (top panel) or 2D (bottom panel) plots for tracking in 2D or 3D respectively. The local maxima in these plots are taken as hypotheses of possible paths forward.

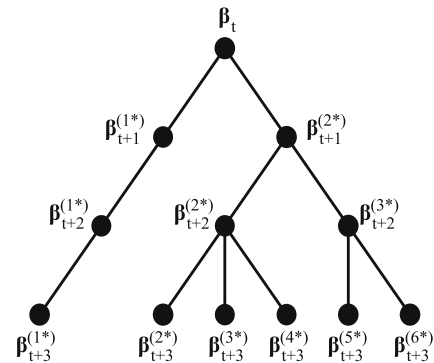


Fig. 7. An example of a multiple hypothesis tracking tree with search depth 3. Each node in the tree represents a local maxima in the prediction scores and each leaf represents a possible path forward from the current point β_t .

4.3. Branch detection

To detect a bifurcation, a clustering is performed on the spatial coordinates of the leaves of the tracking tree. A similar approach has previously been used in Florin et al. (2005). In this work, we use a spectral clustering algorithm (Chung, 1997). First, a symmetric similarity matrix containing a measure of similarity between leaves i and j is constructed as follows:

$$S_{ij} = S_{ji} = e^{-2 \frac{\|\mathbf{x}_i - \mathbf{x}_j\|}{r_i + r_j}} \quad (16)$$

where \mathbf{x}_i and \mathbf{x}_j are the spatial coordinates and r_i and r_j are the radii, respectively, viz. the similarity is based on the absolute spatial distance divided by the average vessel radius. Next, an eigen-decomposition of the Laplacian matrix $\mathbf{L} = \mathbf{D} - \mathbf{S}$ is performed, where \mathbf{D} is a diagonal matrix with entries $\mathbf{D}_{ii} = \sum_j S_{ij}$. The second smallest eigenvector of \mathbf{L} determines the clusters: the indexes for which the eigenvector adopt negative values define one cluster and the indexes with positive values define the other cluster. If the distance between the leaves with the highest prediction scores within each cluster is larger than the current vessel diameter, a junction has been passed.

4.4. Summary

Here, we summarize the main steps and parameters in the MHT algorithm. The algorithm consists of two phases that are iterated during the tracking: building the search tree (cf. Fig. 7) and evaluating the tree to determine the next tracking step. The search tree is built using a recursive approach as outlined in Algorithm 1 and a step is then taken according to Algorithm 2. The termination threshold in Algorithm 2 ensures that, on average, the tracked paths resembles a vessel. If not, the tracking is terminated. The pruning threshold in Algorithm 1 weeds out the poorest predictions but should be set liberally enough to allow occasional steps with low model fits. As a rule of thumb, the termination threshold should be twice as high as the pruning threshold. When the image noise is spatially uncorrelated, a termination threshold of 3 works well. Another important parameter is the search depth. As demonstrated in the Results section, the tracking performance improves with increasing search depth. On the other hand, the search tree and the computational effort grow quickly with increased depth. A search depth of 3 or 4 generally gives a good tradeoff. The length of each step in the tracking is set to 1.5 times the local vessel radius. A detailed discussion about the choice of step length can be found in (Lee et al., 2007). The number of predictions and how widely they are distributed ($\pm\alpha^\circ$) must also be set, cf. Fig. 5. $\alpha = 60^\circ$ is generally sufficient to capture bifurcations. A spacing of 20° degrees between predictions is recommended to yield a total of 7 predictions per image dimension. Finally, the width of the spatial weight function in Eq. (6) (fixed here to $2r$ and $4r$ along and across the vessel, respectively) influences the tracking performance. A larger window improve noise robustness albeit at the expense of higher computational costs.

Algorithm 1. MHT: Building the search tree

- 1: Start with a vessel segment with parameters β_t .
- 2: Produce a number of predictions of the next vessel segment by placing trial models $\beta_{t+1}^{(i)}$ evenly spaced on a sphere in front of the current segment (cf. Section 4.1).
- 3: For each prediction, calculate a score $s(\beta_{t+1}^{(i)})$ describing how well the model fits the image data (cf. Section 3.4).
- 4: Find the local maxima $\beta_{t+1}^{(j^*)}$ in the score pattern (cf. Fig. 6).
- 5: Fit the vessel model parameters in $\beta_{t+1}^{(j^*)}$ to the image data (cf. Section 3.3).
- 6: Discard models for which the scores $s(\beta_{t+1}^{(j^*)})$ do not survive a pruning threshold.
- 7: If the pre-defined search depth has not been reached, start from Step 1 for all surviving predictions.

Algorithm 2. MHT: Evaluating the search tree

- 1: Average the scores of the model segments leading to each leaf of the search tree.
- 2: Discard leaves for which the average scores do not survive a termination threshold. If no leaves survive, terminate the tracking of the current branch and go to the next. Otherwise continue to Step 3.
- 3: Make a bifurcation detection (cf. Section 4.3). If a bifurcation is found, store the origin of one of the branches to be pursued later.
- 4: Take a step towards the leaf with the highest average score.
- 5: Rebuild the search tree from the new point according to Algorithm 1.

5. Results

The multiple hypothesis tracking algorithm and the vessel template model described in the previous sections were implemented in C++ and made available as a module in the free medical image processing and visualization software MeVisLab.¹ In the following sections, the MHT algorithm is evaluated and demonstrated using both synthetic and real data.

5.1. Synthetic data

To demonstrate the improved robustness of the MHT approach, a 3D spiral with small gaps simulating low-contrast areas was generated, see Fig. 8. The radius was 0.75 voxels and the spiral was embedded in a $250 \times 250 \times 70$ voxels large image. The spiral had an intensity of 1 and the background intensity was 0. Gaussian noise with a standard deviation of 0.25 was added to the image prior to tracking. The MHT using the vessel template model was applied using search depths between 1 and 6. In addition, a single hypothesis approach was applied, in which only a single prediction was placed along the tangential line, cf. Fig. 5. A termination threshold of 3 was used in all cases (cf. Eq. (14) and Algorithm 2).

The tracking was initiated at the outer arm as shown by the arrow in Fig. 8c, and the procedure was repeated 1000 times with different noise realizations. As a performance indicator, the amount of the spiral that was segmented as percentage of the total spiral length was measured. The median lengths over the 1000 runs are presented in Fig. 9. The trend shows that the segmentation success increases with increased search depth, from 17% for search depth 1 to 99% for search depth 6. The explanation for this improvement is the increased noise robustness and the ability to bridge the gaps with larger search depths. Another important observation is that the single hypothesis tracking performs better than the MHT with search depth 1 for this data set. This is a side effect of the extensive sampling in the MHT, which gives improved tracking sensitivity but also a higher risk of finding stray paths in the noise. Paired *t*-tests show that the tracking improvement is statistically significant with a significance $p < 0.0001$ for search depths up to 4, whereas the improvement for higher search depths is less significant. An explanation may be that a depth of 4 is enough to bridge the gaps in the spiral robustly.

To further demonstrate the behavior of the MHT and the vessel template model in a few typical situations, three additional 3D simulated data sets are used. Volume renderings of the synthetic 3D data are shown in the top row of Fig. 10. From left to right in this figure, the shapes mimic a vessel with varying radius, a vessel with a neighboring structure with similar intensity, and a tree with bifurcations. In all cases, the synthetic objects have an intensity value of 1 and the background a value of 0, i.e., the generated volumes are binary. Prior to tracking, Gaussian noise with a standard deviation of 0.25 was added to the data. The leftmost column in Fig. 10 shows the segmentation of a vessel segment with varying radius. The tracking steps taken are shown in Fig. 10d. Note that the step length decreases with the vessel radius. A surface reconstruction of the tracking result is shown in Fig. 10g. Because a 3D template cylinder is used as vessel model, the estimated parameters, including the radius, will be smoothed along the vessel. In the middle column of Fig. 10, the tracking of a synthetic vessel lying on a sphere is shown. This example demonstrates that

¹ <http://www.mevislab.de>.

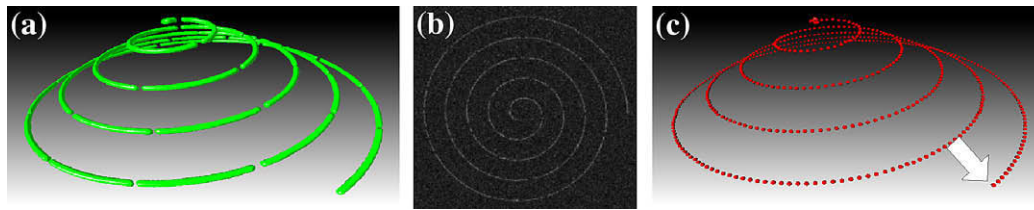


Fig. 8. (a) Volume rendering of a synthetic 3D spiral with a radius of 0.75 voxels. (b) The spiral was embedded in Gaussian noise. The image shows a maximum intensity projection along the z-axis of the image volume. (c) Example centerline points tracked with the MHT method.

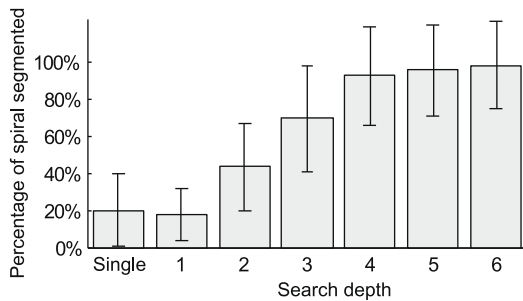


Fig. 9. Median percentage of the spiral in Fig. 8 that was segmented over 1000 runs with different noise realizations. From left to right, the bars show the performance of a single hypothesis tracking and the MHT with search depths from 1 to 6. The lines show the mean absolute deviations.

the proposed tracking algorithm is also able to segment vessels in the presence of adjacent structures of similar intensity, which in this case would be impossible using a method without a strong vessel model, e.g., a region growing or a level-set method. The surface and the sphere are shown in Fig. 10h. The right column of Fig. 10 shows the ability to find branches using a synthetically generated tree.

5.2. CT angiography data – coronary arteries

Segmentation of the coronary arteries that supply the heart muscle is essential for detecting and analyzing occlusions and stenoses that may lead to a heart infarct. The goal of the challenge 3D segmentation in the clinic: A Grand Challenge II – Coronary Artery

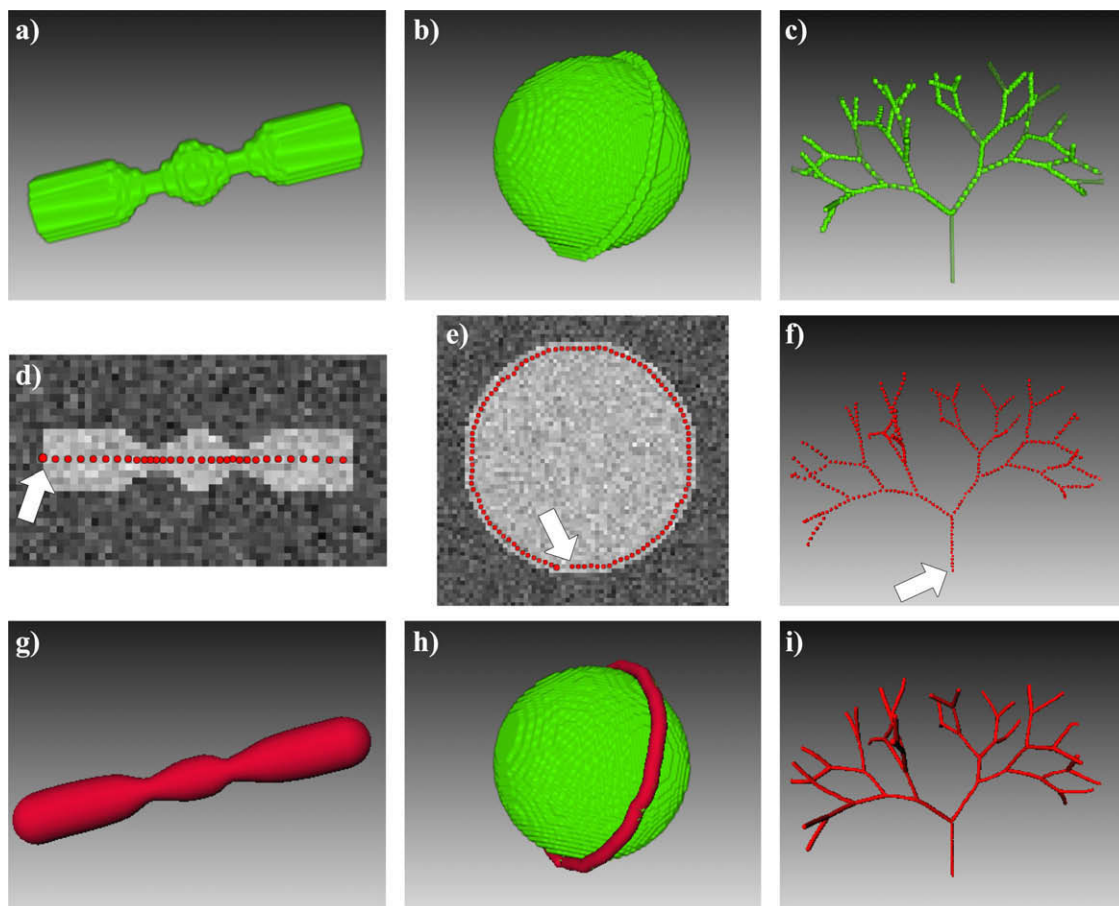


Fig. 10. Segmentation of synthetic 3D shapes using a tracking started at the arrows. Upper row: Volume renderings of the synthetic shapes. Middle row: Steps taken by the tracking algorithm. Bottom row: Surface reconstructions of the segmented vessels. Left column: Vessel with varying radius. The data set size is $31 \times 55 \times 31$ voxels. Middle column: A vessel put on the surface of a sphere showing the ability to track in the presence of an adjacent structure with similar image intensity. The sphere has a diameter of 50 voxels and the vessel a diameter of 3 voxels. The data set size is $81 \times 81 \times 81$ voxels. Right column: A vessel tree showing the ability to detect bifurcations. The vessel branches are 3 voxels in diameter and the data set size is $256 \times 256 \times 256$ voxels.

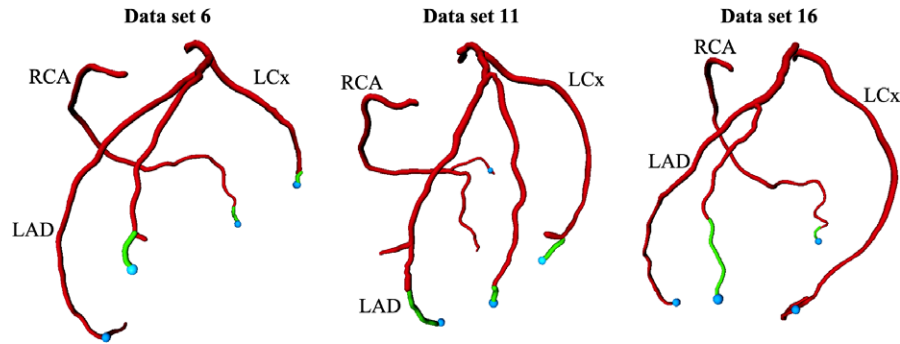


Fig. 11. Coronary artery reconstructions of three cardiac angiography data sets. The blue spheres indicate the end points of the target coronary arteries to segment in the 3D segmentation in the clinic: A Grand Challenge II – Coronary Artery Tracking competition. The red vessel parts were segmented using the MHT and the green parts using the minimal path approach. RCA = right coronary artery, LAD = left anterior descending artery and LCx = left circumflex artery. (For interpretation of the references to colour in this figure legend, the reader is referred to the web version of this article.)

*Tracking*² (Metz et al., 2008) is to track the coronary artery centerlines as accurately as possible. In the context of this competition, an image database is available,³ which consists of 32 CT angiography data sets, acquired using 64-row and dual-source CT scanners. Moreover, it is possible to submit algorithmic segmentations for evaluation with respect to ground-truth centerlines manually drawn by three medical experts. For eight of the data sets in the image database, the ground-truth centerlines are publicly available (data set numbers 0–7), but not for the remaining 24 data sets (data set numbers 8–31).

To address the entire range of vessel sizes and contrasts in cardiac CT angiography data sets, two algorithm classes in Fig. 1 were combined in this work, i.e., the MHT was combined with a standard minimal path algorithm (Deschamps and Cohen, 2001) into an interactive approach for segmenting the coronary arteries. The segmentation process was as follows: two seed points for the MHT were manually set in the aortic ostia, i.e., at the base of the right and left coronary artery main stems. A search depth of 4 in the MHT was used. If the MHT terminated prematurely, further seed points could be added. At places where the MHT was not able to track, the minimal path approach (requiring manually selected start and end points) was used to complement the segmentation. The coronary arteries in the 32 data sets described above were segmented and the results were submitted for evaluation. Partial results have been presented in the context of the 3D segmentation in the clinic: A Grand Challenge II – Coronary Artery Tracking competition (Friman et al., 2008).

Examples of reconstructions of the coronary arteries are shown in Fig. 11, in which the red parts were segmented using the MHT and the green parts with the minimal path algorithm. Accuracy results for all 32 data sets are presented in Table 1. Averaged across all data sets, the overlap (defined as measure *OV* in the competition description Metz et al., 2008) with the human expert segmentations is 98.7%. The accuracy (defined as measure *AD* in Metz et al., 2008), i.e., average distance to the ground-truth centerlines, is 0.25 mm. This should be compared with the voxel size of about $0.6 \times 0.6 \times 0.8$ mm. These are the highest scores achieved among the 13 algorithms, both fully automatic as well as semi-automatic, that have been tested against the competition image data base at the time of writing (Schaap et al., 2009). The average interaction per vessel for the hybrid MHT/minimal path approach is 1.5 clicks for the MHT and 1 minimal path. About 80–90% of the vessels were segmented with the MHT, the minimal path approach was used for the final 10–20%, as is demonstrated in Fig. 11. The average segmentation time is about 5 min per data set, of which the actual compu-

Table 1

Results for the MHT and minimal path approach for segmenting the coronary arteries in 32 CT angiography image volumes. The overlap and accuracy measures indicate the performance compared to human expert segmentations. For the training data sets (numbers 0–7), the ground-truth segmentations were available. For the testing data sets (numbers 8–31), the ground-truth segmentations were not available to the authors.

Data set numbers	Overlap (%)	Accuracy (mm)
<i>Training data</i>		
0	99.6	0.33
1	100.0	0.23
2	100.0	0.20
3	98.6	0.29
4	97.7	0.21
5	99.2	0.30
6	99.9	0.19
7	99.5	0.25
<i>Testing data</i>		
8	92.5	0.39
9	100.0	0.16
10	99.4	0.23
11	96.0	0.33
12	99.2	0.24
13	98.6	0.23
14	99.9	0.24
15	99.0	0.19
16	99.3	0.23
17	99.4	0.32
18	98.8	0.20
19	100.0	0.25
20	99.4	0.30
21	100.0	0.17
22	99.9	0.21
23	100.0	0.23
24	99.3	0.18
25	97.9	0.25
26	92.2	0.54
27	96.1	0.35
28	99.8	0.20
29	99.3	0.19
30	99.0	0.21
31	99.6	0.15
Average	98.7	0.25

tational time is just a small fraction – a few seconds per vessel on a standard laptop computer with a 1.83 GHz dual-core processor.

5.3. CT angiography data – liver arteries

In liver surgery planning, the liver arteries play an important role in determining optimal resections and in predicting blood sup-

² Carried out as a workshop at the 11th International Conference on Medical Image Computing and Computer Assisted Intervention (MICCAI'08).

³ <http://coronary.bigr.nl/>.

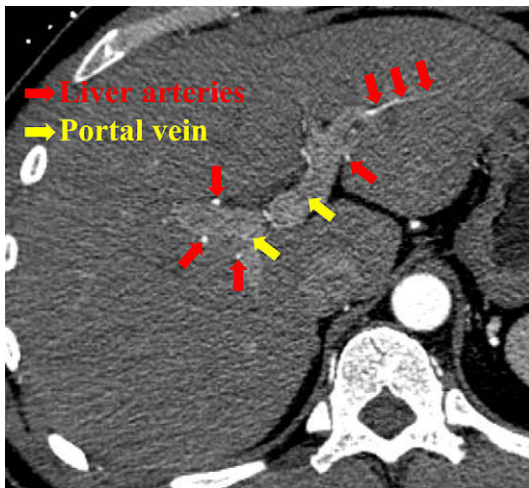


Fig. 12. A slice from the arterial phase of a CT angiography data set. The larger portal veins are indicated with yellow arrows and the smaller arteries with red arrows. (For interpretation of the references to colour in this figure legend, the reader is referred to the web version of this article.)

ply to remaining liver tissue. In contrast to the coronary arteries, calcifications and stenoses are rarely present in the liver arteries and the clinically relevant factor for liver surgery planning is the vessel locations. To visualize the liver vessel systems, 3D CT angiography is the standard image acquisition method. The acquired image volumes are typically of the size $512 \times 512 \times 400$ voxels with a voxel size of about $0.8 \times 0.8 \times 0.6$ mm. The main problem in segmenting the liver arteries is that they are small and very poorly contrasted in the CT data, see Fig. 12. Another complicating factor is that the arteries run next to the larger portal veins, which increases the risk of segmentation leakage. Presently, at our institute, the liver arterial system is routinely segmented completely by hand for surgical planning purposes, a procedure that takes a trained expert up to 30 min. To the best of our knowledge, no automatic or semi-automatic algorithm for segmenting the liver arteries has previously been presented. To address this problem, we again devise a hybrid approach in which the vessel segmentation is initiated with a region growing and finalized with the MHT. The region growing is initiated in the two main arteries entering the liver from the aorta. These two stem arteries are larger and more highly contrasted than the distal vessel branches. A Gaussian pre-smoothing ($\sigma = 0.75$ voxels) is used for the region growing and the threshold is conservatively set to avoid leakage. Next, tracking seeds are manually placed in vessel branches that were not found by the region growing. The tracking is applied to the original data, i.e., no pre-processing or smoothing is used. Again, a search depth of 4 is used in the MHT.

A segmentation example of a CT angiography volume of the liver is shown in Fig. 13. The yellow part of the vessel system was segmented using the region growing and the blue parts using the MHT. In Fig. 14, the centerlines of eight additional liver artery systems are shown. The blue centerlines show vessels that were manually delineated by medical experts. The red centerlines show semi-automatically segmented vessels (one click per branch). The centerlines have been shifted relative to each other to facilitate visualization. There are a few vessel segments which the tracking is unable to find. These are typically located in areas affected by imaging artifacts or where the vessel contrast is so low that a human can infer their existence only via other contextual factors such as proximity to a larger vein. However, the tracking is able to segment a major part of the arterial systems accurately, and only minor manual editing is necessary compared to a fully manual

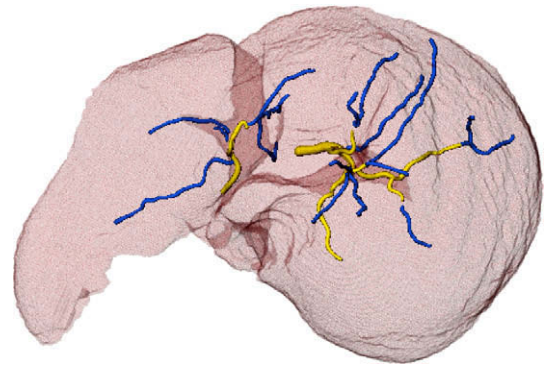


Fig. 13. A segmented liver artery system. The yellow parts were segmented using a region growing and the blue parts were segmented using the MHT. (For interpretation of the references to colour in this figure legend, the reader is referred to the web version of this article.)

segmentation. The tracking requires about 1–2 s per vessel on a standard laptop computer 1.83 GHz dual-core processor.

6. Discussion

The proposed MHT method may be considered a deterministic alternative to the recently published Bayesian particle filters (Florin et al., 2005; Shim et al., 2006; Schaap et al., 2007). Whereas the particle filters stochastically sample their way forward, the MHT samples its way with systematic sweeps, cf. Fig. 5. Where the particle filter furnishes a probability distribution of possible vessel paths, the MHT uses the tracking search tree, cf. Fig. 7. An advantage of the MHT over the particle filter is its computational complexity, an important factor when the method is to be used in practice. The speed advantage derives from its systematic sampling, which is more efficient than a stochastic sampling. Concretely, the particle filters presented by Florin et al. (2005), Shim et al. (2006), and Schaap et al. (2007) evaluate 1000, 500, and 500 model instances (i.e., particles) in each tracking step respectively. The MHT presented here uses about 100 model evaluations in 3D for the prediction and fitting steps. For small vessels, requiring small vessel template functions, the MHT can run at interactive speed. Furthermore, it should be stressed that the MHT principle can be employed with any vessel model previously proposed for vessel tracking (Aylward and Bullitt, 2002; McIntosh and Hamarneh, 2006; Behrens et al., 2003; Florin et al., 2005; Shim et al., 2006; Krissian et al., 2006; Tyrrell et al., 2007; Schaap et al., 2007; Lee et al., 2007; Rossignac et al., 2007; Wörz and Rohr, 2007; Wong and Chung, 2007).

The vessel profile presented in Eq. (1) is a heuristic mathematical construction for unsmoothed image data. An alternative empirical profile model could be found by analyzing the vessel cross-sections in the manually segmented data, although this would require the fitting problem to be solved differently, as such a model would not be analytically differentiable. The advantage of mathematically defined template models, including, for example, the ones described in Noordmans and Smeulders (1998), La Cruz et al. (2004) and Wörz and Rohr (2007), with closed-form expressions of the derivatives, is that a high fitting accuracy can be obtained, as shown by the subvoxel precision in the segmented coronary centerlines in Section 5.2. As noted by one reviewer, the particular profile function in Eq. (1) has an undesired property in that the slope depends on the radius. The effect is negligible for the small vessels considered in this work, but not for larger vessels such as the aorta or major veins. Again, with modular construction of the vessel template model in Eq. (4) it is straightforward to switch profile function.

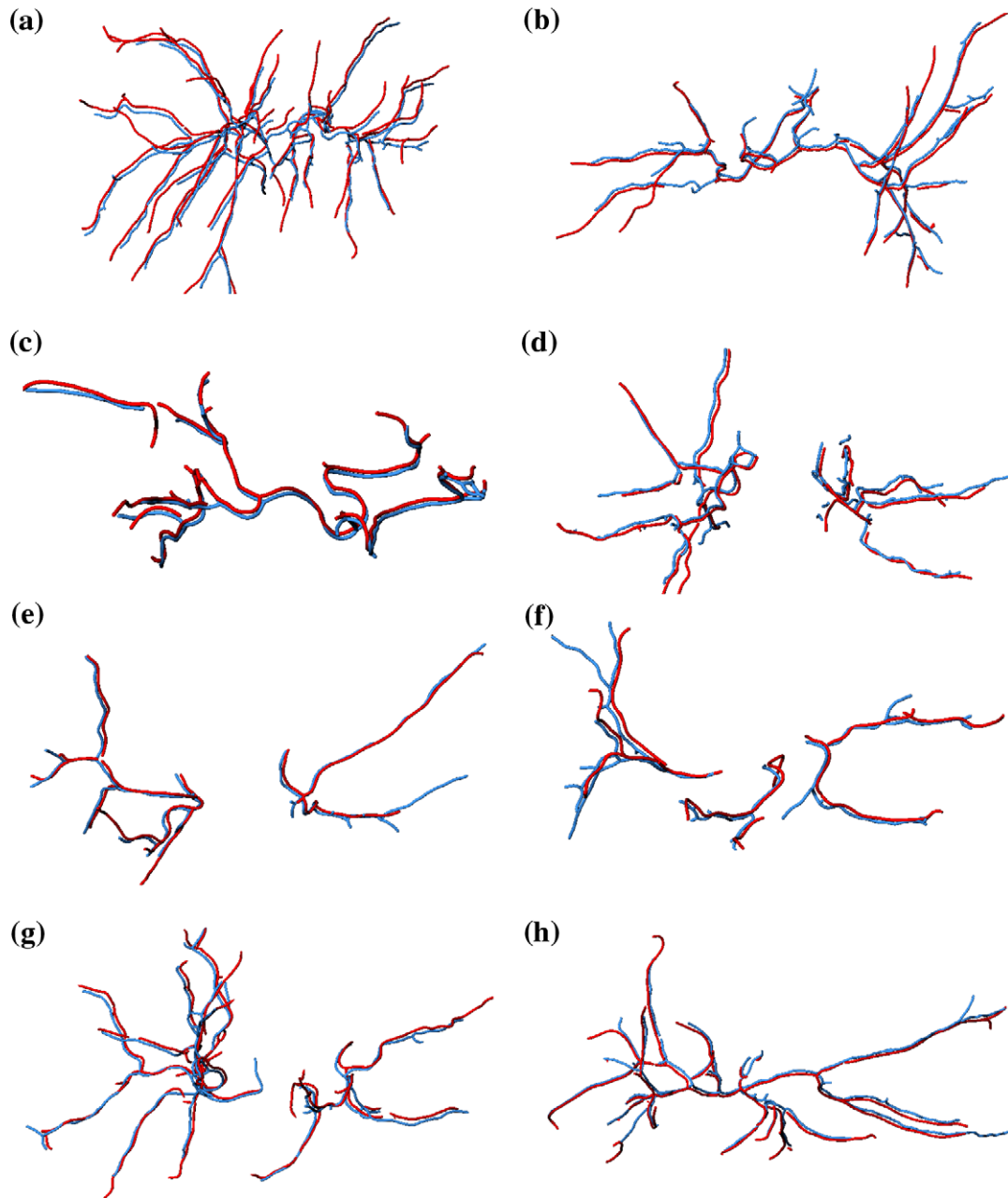


Fig. 14. Comparison between manually and semi-automatically segmented liver arteries. (a)–(h) show eight different liver artery systems. The blue vessels show the centerlines of the manual segmentation. The red vessels are the result of the hybrid region growing and tracking approach. The centerlines have been intentionally shifted relative to each other to facilitate visualization. (For interpretation of the references to colour in this figure legend, the reader is referred to the web version of this article.)

The vessel template model does not only assume a certain shape of the vessel itself, e.g., the vessel profile, but also a homogeneous image neighborhood around the vessel. This strong modeling makes it possible to segment very weakly contrasted vessels, such as the liver arteries. However, problems arise in the presence of neighboring structures or inhomogeneous background. For example, premature terminations were sometimes observed when segmenting the coronary arteries for cases in which the artery was either running along the heart/lung interface or close to the highly contrasted blood pool. Such problems can often be solved by means of simple image pre-processing. Touching vessels and vessel bifurcations are more difficult to handle. Vessel bifurcations become an Achilles' heel when the vessel is modeled as an object with a well-defined centerline, because this model fits poorly at

bifurcations, which may lead to termination of the tracking or the missed detection of one vessel branch. The MHT approach ameliorates the problem to some extent, as it can work with liberal termination thresholds. Still, a general branching detection strategy remains a subject of future research. One potential approach may be to extend the sampling pattern in Fig. 5 to include steps of different lengths in the MHT to obtain a better sampling of the area in front of the current tracking point. An interesting search pattern related to this approach has recently been presented by Zambal et al. (2008). The advantage of including longer step lengths is that tracking is more likely to jump across the problematic bifurcation area and put predictions in the post-bifurcation branches, from which the tracking can continue. The problem of touching vessels can arise when the arterial and venous vessel sys-

tems are closely intertwined. This is a general problem that may require additional pre- or post-processing, e.g., in the form image gradient or graph representation operations.

The clinical utility of the MHT is in this work demonstrated by applying it to cardiac and liver CT angiography data. Within the context of the *3D segmentation in the clinic: A Grand Challenge II – Coronary Artery Tracking* competition, the MHT approach achieved the highest scores among 13 different segmentation methods. Although a few of these methods are fully automatic, making a direct comparison impossible, the results show that highly accurate segmentations can be obtained with the MHT and the vessel template model. Furthermore, the MHT approach is able to introduce some degree of automation in the hitherto fully manual liver artery segmentation process. The fact that the MHT runs at interactive speed is also clinically relevant.

7. Conclusions

The main contributions in this work are as follows: a multiple hypothesis tracking framework for 3D vessel segmentation has been introduced, and it has been shown how this tracking procedure improves the tracking performance. The MHT framework can be applied using many different vessel models. The specific vessel model introduced in this work is a mathematically tractable template model that can be analytically fitted to the image data. A statistically motivated criterion for assessing the model fit has also been derived. The proposed method achieves a high centerline detection accuracy, as demonstrated using 32 cardiac CT angiography data sets in the *3D segmentation in the clinic: A Grand Challenge II – Coronary Artery Tracking* competition. Moreover, an efficient semi-automatic segmentation of the liver arteries has been shown for the first time. Finally, the tracking algorithm has been released as free software to facilitate future use and comparisons.

Appendix A

In this appendix, the partial derivatives of the vessel template model $T(\mathbf{x}; r, \mathbf{x}_0, \hat{\mathbf{v}})$ with respect to changes in the radius (r), center point (\mathbf{x}_0) and direction ($\hat{\mathbf{v}}$) are derived. These derivatives are required in the fitting process described in Section 3.3. For convenience, first the expressions for the template model from Section 2 are repeated.

A.1. Vessel template equations

The template function (cf. Eq. (4)) is

$$T(\mathbf{x}; r, \mathbf{x}_0, \hat{\mathbf{v}}) = p \circ d^2(\mathbf{x}) = p(d^2(\mathbf{x}; \mathbf{x}_0, \hat{\mathbf{v}}); r) \quad (17)$$

where $p(d^2; r)$ is the vessel profile function

$$p(d^2; r) = \frac{r^\gamma}{(d^2)^{\gamma/2} + r^\gamma} \quad \text{with } \gamma = 8 \quad (18)$$

and $d^2(\mathbf{x}; \mathbf{x}_0, \hat{\mathbf{v}})$ is a distance function to a straight line

$$d^2(\mathbf{x}; \mathbf{x}_0, \hat{\mathbf{v}}) = \|\mathbf{x} - \mathbf{x}_0\|^2 - [\hat{\mathbf{v}}^T(\mathbf{x} - \mathbf{x}_0)]^2 \quad (19)$$

A.2. Radius derivative: $\frac{\partial T}{\partial r}$

A change in radius affects the template function as follows

$$\frac{\partial T}{\partial r} = \frac{\partial p}{\partial r} = \frac{\gamma}{r} p(1 - p) \quad (20)$$

where T is short for $T(\mathbf{x}; r, \mathbf{x}_0, \hat{\mathbf{v}})$ in Eq. (17) and p is short for $p(d^2; r)$ in Eq. (18).

A.3. Rotation derivative: $\frac{\partial T}{\partial \theta}$ and $\frac{\partial T}{\partial \phi}$

As discussed in Section 3.3.2, if the vessel direction $\hat{\mathbf{v}}$ is expressed in spherical coordinates, i.e. in 3D

$$\hat{\mathbf{v}}(\theta, \phi) = \begin{bmatrix} \sin(\phi) \cos(\theta) \\ \sin(\phi) \sin(\theta) \\ \cos(\phi) \end{bmatrix} \quad (21)$$

where θ is the azimuth angle in the xy -plane from the x -axis ($0 \leq \theta < 2\pi$) and ϕ is the polar angle from the z -axis ($0 \leq \phi \leq \pi$), a rotation is simply a change in θ and ϕ . The derivatives with respect to these angles are found via the chain rule

$$\frac{\partial T}{\partial \theta} = \frac{\partial p}{\partial d^2} \left(\frac{\partial d^2}{\partial \hat{\mathbf{v}}} \right)^T \left(\frac{\partial \hat{\mathbf{v}}}{\partial \theta} \right) \quad (22)$$

where

$$\frac{\partial p}{\partial d^2} = -\frac{\gamma}{2r^\gamma} (d^2)^{\frac{\gamma}{2}-1} p^2 \quad (23)$$

$$\frac{\partial d^2}{\partial \hat{\mathbf{v}}} = -2[\hat{\mathbf{v}}^T(\mathbf{x} - \mathbf{x}_0)](\mathbf{x} - \mathbf{x}_0) \quad (24)$$

and

$$\frac{\partial \hat{\mathbf{v}}}{\partial \theta} = \sin(\phi)[- \sin(\theta), \cos(\theta), 0]^T \quad (25)$$

The derivative of $T(\mathbf{x}; r, \mathbf{x}_0, \hat{\mathbf{v}})$ with respect to ϕ , $\frac{\partial T}{\partial \phi}$, is calculated analogously with $\frac{\partial \hat{\mathbf{v}}}{\partial \phi} = [\cos(\phi) \cos(\theta), \cos(\phi) \sin(\theta), -\sin(\phi)]^T$. For 2D tracking in the xy -plane, ϕ is fixed to $\phi = \pi/2$.

A.4. Translation derivative: $\frac{\partial T}{\partial \mathbf{x}_0}$

A translation of the vessel template is a change in the center point \mathbf{x}_0 and

$$\frac{\partial T}{\partial \mathbf{x}_0} = \frac{\partial p}{\partial d^2} \frac{\partial d^2}{\partial \mathbf{x}_0} \quad (26)$$

where $\frac{\partial p}{\partial d^2}$ is given in Eq. (23) and

$$\frac{\partial d^2}{\partial \mathbf{x}_0} = -2(\mathbf{x} - \mathbf{x}_0) + 2[\hat{\mathbf{v}}^T(\mathbf{x} - \mathbf{x}_0)]\hat{\mathbf{v}} \quad (27)$$

Translating the template along the template direction $\hat{\mathbf{v}}$ produces no change, which can be seen mathematically as $\hat{\mathbf{v}}^T \left(\frac{\partial T}{\partial \mathbf{x}_0} \right) \equiv 0$. Hence, only translations orthogonal to the vessel direction are considered. In Section 3.2, the unit vectors $\hat{\mathbf{u}}_1$ and $\hat{\mathbf{u}}_2$ were introduced. $\hat{\mathbf{u}}_1$ and $\hat{\mathbf{u}}_2$ are orthogonal to both $\hat{\mathbf{v}}$ and each other, i.e., $\hat{\mathbf{v}} \perp \hat{\mathbf{u}}_1 \perp \hat{\mathbf{u}}_2$. That is, $\hat{\mathbf{u}}_1$ and $\hat{\mathbf{u}}_2$ span the plane to which $\hat{\mathbf{v}}$ is the normal vector. The pair of $\hat{\mathbf{u}}_1$ and $\hat{\mathbf{u}}_2$ is not unique, but any pair perpendicular to both each other and $\hat{\mathbf{v}}$ will suffice. The derivatives of the vessel template with respect to a translation along $\hat{\mathbf{u}}_1$ and $\hat{\mathbf{u}}_2$ are given by $\hat{\mathbf{u}}_1^T \left(\frac{\partial T}{\partial \mathbf{x}_0} \right)$ and $\hat{\mathbf{u}}_2^T \left(\frac{\partial T}{\partial \mathbf{x}_0} \right)$ respectively. For 2D tracking, only $\hat{\mathbf{u}}_1$ is used.

References

- Adams, R., Bischof, L., 1994. Seeded region growing. IEEE Transactions on Pattern Analysis and Machine Intelligence 16 (6), 641–647.
- Aylward, S.R., Bullitt, E., 2002. Initialization, noise, singularities, and scale in height ridge traversal for tubular object centerline extraction. IEEE Transactions on Medical Imaging 21 (2), 61–75.
- Behrens, T., Rohr, K., Stiehl, H.S., 2003. Robust segmentation of tubular structures in 3-D medical images by parametric object detection and tracking. IEEE Transactions on Systems, Man, and Cybernetics, Part B: Cybernetics 33 (4), 554–561.
- Bhalerao, A., Thönnies, E., Kendall, W., Wilson, R., 2001. Inferring vascular structure from 2D and 3D imagery. In: Medical Image Computing and Computer-assisted Intervention (MICCAI'01), 2001, pp. 820–828.

- Björck, Å., 1996. Numerical Methods for Least Squares Problems. SIAM.
- Blackman, S.S., 2004. Multiple hypothesis tracking for multiple target tracking. *IEEE Aerospace and Electronic Systems Magazine* 19 (1), 5–18.
- Bühler, K., Felkel, P., Cruz, A.L., 2003. Geometric methods for vessel visualization and quantification – a survey. In: Brunnett, H.M.G., Hamann, B. (Eds.), *Geometric Modelling for Scientific Visualization*. Springer, pp. 399–421.
- Canero, C., Radeva, P., 2003. Vesselness enhancement diffusion. *Pattern Recognition Letters* 24 (16), 3141–3151.
- Chaudhuri, S., Chatterjee, S., Katz, N., Nelson, M., Goldbaum, M., 1989. Detection of blood vessels in retinal images using two dimensional matched filters. *IEEE Transactions on Medical Imaging* 8 (3), 263–269.
- Chen, J., Amini, A.A., 2004. Quantifying 3-D vascular structures in MRA images using hybrid PDE and geometric deformable models. *IEEE Transactions on Medical Imaging* 23 (10), 1251–1262.
- Chung, F.R.K., 1997. Spectral Graph Theory. American Mathematical Society.
- Deschamps, T., Cohen, L.D., 2001. Fast extraction of minimal paths in 3D images and application to virtual endoscopy. *Medical Image Analysis* 5 (4), 281–299.
- Deschamps, T., Cohen, L.D., 2002. Fast extraction of tubular and tree 3D surfaces with front propagation methods. In: 16th International Conference on Pattern Recognition (ICPR'02), 2002, pp. 731–734.
- Draper, N.R., Smith, H., 1998. *Applied Regression Analysis*, 3rd ed. Wiley, New York.
- Florin, C., Paragios, N., Williams, J., filters, Particle, 2005. A quasi-Monte Carlo solution for segmentation of coronaries. In: *Medical Image Computing and Computer-assisted Intervention (MICCAI'05)*. LNCS, vol. 3749. Springer, Berlin/Heidelberg, pp. 246–253.
- Frangi, A.F., Niessen, W.J., Vincken, K.L., Viergever, M.A., 1998. Multiscale vessel enhancement filtering. In: *Medical Image Computing and Computer-assisted Intervention (MICCAI'98)*, 1998, pp. 130–137.
- Friman, O., Hindennach, M., Peitgen, H.-O., 2008. Template-based multiple hypotheses tracking of small vessels. In: *Proc. IEEE Int. Symp. Biom. Imaging (ISBI'08)*, 2008, pp. 1047–1050.
- Friman, O., Kühnel, C., Peitgen, H.-O., 2008. Artery centerline extraction using multiple hypothesis tracking and minimal paths. In: *3D Segmentation in the Clinic: A Grand Challenge II Workshop, Medical Image Computing and Computer Assisted Intervention (MICCAI'08)*, 2008.
- Gill, P.E., Murray, W., 1978. Algorithms for the solution of the nonlinear least-squares problem. *SIAM Journal on Numerical Analysis* 15 (5), 977–992.
- Gooya, A., Liao, H., Matsumiya, K., Masamune, K., Dohi, T., 2007. Effective statistical edge integration using a flux maximizing scheme for volumetric vascular segmentation in MRA. In: *Information Processing in Medical Imaging (IPMI'07)*. Springer, Berlin/Heidelberg, pp. 86–97.
- Kirbas, C., Quek, F., 2004. A review of vessel extraction techniques and algorithms. *ACM Computing Surveys* 36 (2), 81–121.
- Krissian, K., 2002. Flux-based anisotropic diffusion: application to enhancement of 3D angiogram. *IEEE Transactions on Medical Imaging* 22 (11), 1440–1442.
- Krissian, K., Malandain, G., Ayache, N., Vaillant, R., Troussset, Y., 2000. Model based detection of tubular structures in 3D images. *Computer Vision and Image Understanding* 80 (2), 130–171.
- Krissian, K., Wu, X., Luboz, V., 2006. Smooth vasculature reconstruction with circular and elliptic cross sections. In: *Medicine Meets Virtual Reality Conference (MMVR'06)*, 2006.
- La Cruz, A., Straka, M., Köchl, A., Sránek, M., Gröller, E., Fleischmann, D., 2004. Non-linear model fitting to parameterize diseased blood vessels. In: *Proceedings of IEEE Visualization*, 2004, pp. 393–400.
- Lee, J., Beighley, P., Ritman, E., Smith, N., 2007. Automatic segmentation of 3D micro-CT coronary vascular images. *Medical Image Analysis* 11 (6), 630–647.
- Lesage, D., Angelini, E.D., Bloch, I., Funka-Lea, G., 2009. A review of 3D vessel lumen segmentation techniques: models, features and extraction schemes. *Medical Image Analysis* 13 (6), 819–845.
- Lorigo, L.M., Faugeras, O.D., Grimson, W.E.L., Keriven, R., Kikinis, R., Nabavi, A., Westin, C.-F., 2001. CURVES: curve evolution for vessel segmentation. *Medical Image Analysis* 5 (3), 195–206.
- Manniesing, R., Niessen, W.J., 2004. Local speed functions in level set based vessel segmentation. In: *Medical Image Computing and Computer-assisted Intervention (MICCAI'04)*, vol. 3217 of LNCS, 2004, pp. 475–482.
- Manniesing, R., Viergever, M.A., Niessen, W.J., 2006. Vessel enhancing diffusion – a scale space representation of vessel structures. *Medical Image Analysis* 10 (6), 815–825.
- Manniesing, R., Velthuis, B.K., van Leeuwen, M.S., van der Schaaf, I.C., van Laar, P.J., Niessen, W.J., 2006. Level set based cerebral vasculature segmentation and diameter quantification in CT angiography. *Medical Image Analysis* 10 (2), 200–214.
- Manniesing, R., Viergever, M.A., Niessen, W.J., 2007. Vessel axis tracking using topology constrained surface evolution. *IEEE Transactions on Medical Imaging* 26 (3), 309–316.
- McIntosh, C., Hamarneh, G., 2006. Vessel crawlers: 3D physically-based deformable organisms for vasculature segmentation and analysis. In: *Proceedings of IEEE Computer Society Conference on Computer Vision and Pattern Recognition (CVPR'06)*, 2006, pp. 1084–1091.
- Metz, C., Schaap, M., van Walsum, T., van der Giessen, A., Weustink, A., Mollet, N., Krestin, G., Niessen, W., 2008. 3D segmentation in the clinic: a grand challenge II – coronary artery tracking. In: *3D Segmentation in the Clinic: A Grand Challenge II Workshop, Medical Image Computing and Computer Assisted Intervention (MICCAI'08)*, 2008.
- Miles, F.P., Nuttall, A.L., 1993. Matched filter estimation of serial blood vessel diameters from video images. *IEEE Transactions Medical Imaging* 12 (2), 147–152.
- Nain, D., Yezzi, A., Turk, G., 2004. Vessel segmentation using a shape driven flow. In: *Medical Image Computing and Computer-assisted Intervention (MICCAI'04)*. LNCS, vol. 3216. Springer, Berlin/Heidelberg, pp. 51–59.
- Noordmans, H.J., Smeulders, A.W.M., 1998. High accuracy tracking of 2D/3D curved line-structures by consecutive cross-section matching. *Pattern Recognition Letters* 19 (1), 97–111.
- O'Brien, J.F., Ezquerro, N.F., 1994. Automated segmentation of coronary vessels in angiographic image sequences utilizing temporal, spatial structural constraints. In: *SPIE Visualization in Biomedical Computing*, 1994, pp. 25–37.
- Olabarriaga, S.D., Breeuwer, M., Niessen, W.J., 2003. Minimum cost path algorithm for coronary artery central axis tracking in CT images. *Medical Image Computing and Computer-assisted Intervention (MICCAI'03)*, vol. 2879. Springer, Berlin/Heidelberg, pp. 687–694.
- Reid, D.B., 1979. An algorithm for tracking multiple targets. *IEEE Transactions on Automatic Control* 24 (6), 843–854.
- Rossignac, J., Whited, B., Slabaugh, G., Fang, T., Unal, G., 2007. Pearling: 3D interactive extraction of tubular structures from volumetric images. In: *Medical Image Computing and Computer-assisted Intervention (MICCAI'07)*, 2007.
- Sato, Y., Nakajima, S., Atsumi, H., Koller, T., Gerig, G., Yoshida, S., Kikinis, R., 1997. 3D multi-scale line filter for segmentation and visualization of curvilinear structures in medical images. In: *1st Joint Conference Computer Vision, Virtual Reality and Robotics in Medicine and Medical Robotics and Computer-Assisted Surgery*, vol. 1205, 1997.
- Schaap, M., Smal, I., Metz, C., van Walsum, T., Niessen, W., 2007. Bayesian tracking of elongated structures in 3D images. In: *Information Processing in Medical Imaging (IPMI'07)*. LNCS, vol. 4584. Springer, Berlin/Heidelberg, pp. 74–85.
- Schaap, M., Metz, C., van Walsum, T., van der Giessen, A., Weustink, A., Mollet, N., Bauer, C., Bogunović, H., Castro, C., Deng, X., Dikici, E., O'Donnell, T., Frenay, M., Friman, O., Hoyos, M.H., Kitslaar, P., Krissian, K., Kühnel, C., Orkisz, M., Luengo-Oroz, M.A., Smedby, O., Styner, M., Szymczak, A., Tek, H., Wang, C., Warfield, S., Zambal, S., Zhang, Y., 2009. Standardized evaluation methodology and reference database for evaluating coronary artery centerline extraction algorithms. *Medical Image Analysis* 13 (5), 701–714.
- Shim, H., Kwon, D., Yun, I.D., Lee, S.U., 2006. Robust segmentation of cerebral arterial segments by a sequential Monte Carlo method: particle filtering. *Comput Methods and Programs in Biomedicine* 84 (2–3), 135–145.
- Suri, J.S., Liu, K., Reden, L., Laxminarayan, S., 2002. A review on MR vascular image processing: skeleton versus non-skeleton approaches: part II. *IEEE Transactions on Information Technology in Biomedicine* 6 (4), 338–350.
- Tyrell, J.A., di Tomaso, E., Fuja, D., Tong, R., Kozak, K., Jain, R.K., Roysam, B., 2007. Robust 3-D modeling of vasculature imagery using superellipsoids. *IEEE Transactions on Medical Imaging* 26 (2), 223–237.
- Vasilevskiy, A., Siddiqi, K., 2002. Flux maximizing geometric flows. *IEEE Transactions on Pattern Analysis and Machine Intelligence* 24 (12), 1565–1578.
- Wan, S.-Y., Higgins, W.E., 2003. Symmetric region growing. *IEEE Transactions on Image Processing* 12 (9), 1007–1015.
- Wink, O., Niessen, W.J., Viergever, M.A., 2000. Fast delineation and visualization of vessels in 3D angiographic images. *IEEE Transactions on Medical Imaging* 19 (4), 337–346.
- Wong, W., Chung, A., 2007. Probabilistic vessel axis tracing and its application to vessel segmentation with stream surfaces and minimum cost paths. *Medical Image Analysis* 11 (6), 567–587.
- Wörz, S., Rohr, K., 2007. Segmentation and quantification of human vessels using a 3-D cylindrical intensity model. *IEEE Transactions on Image Processing* 16 (8), 1994–2004.
- Wörz, S., Rohr, K., 2007. 3D adaptive model-based segmentation of human vessels. In: *Proc. SPIE Medical Imaging 2007: Physiology, Function, and Structure from Medical Images (MI'07)*, 2007.
- Yan, P., Kassim, A.A., 2006. Segmentation of volumetric MRA images by using capillary active contour. *Medical Image Analysis* 10 (3), 317–329.
- Yang, Y., Stillman, A., Tannenbaum, A., Giddens, D., 2007. Automatic segmentation of coronary arteries using Bayesian driven implicit surfaces. In: *4th IEEE International Symposium on Biomedical Imaging (ISBI'07)*, 2007, pp. 189–192.
- Zambal, S., Hladuvka, J., Kanitsar, A., Bühler, K., 2008. Shape and appearance models for automatic coronary artery tracking. In: *3D Segmentation in the Clinic: A Grand Challenge II Workshop, Medical Image Computing and Computer Assisted Intervention (MICCAI'08)*, 2008.